Imaging Low-Energy Ion Outflow in the Auroral Zone

Douglas Rowland[1]*, Michael Collier[1†], John Keller[1], Robert Pfaff[1], Jeffrey Klenzing[1], Jason McLain[1], James Clemmons[2] and James Hecht[3]

[1]NASA Goddard Space Flight Center, Greenbelt, MD, United States, [2]Physics Department, The University of New Hampshire, Durham, NH, United States, [3]The Aerospace Corporation, El Segundo, CA, United States

The VISualizing Ion Outflow via Neutral atom imaging during a Substorm (VISIONS) sounding rocket mission investigated the factors leading to ion outflow following a geomagnetic substorm. *In situ* and remote sensing instrumentation provided complementary measurements that have been combined to yield an in-depth look at the phenomena associated with ion outflow. In particular, the inclusion of instrumentation that provided high spatial and temporal resolution "images" of low-energy neutral atom (ENA) emissions from the nightside auroral zone following a substorm has led to new insights. The observed ENAs were spatially structured, and strongly associated with regions of intense 630.0 nm auroral emissions. The ENAs in the auroral zone were predominantly up-going, consistent with thick-target scattering in the region where the ENA mean free path is close to or less than the atmospheric scale height.

Keywords: magnetosphere-ionosphere coupling, ionosphere, plasma transport, particle energization, ion outflow

1 INTRODUCTION

Ion outflow is one of the most critical two-way feedback mechanisms between the ionosphere/thermosphere and magnetosphere (see, e.g., Welling et al., 2015; Huddleston et al., 2005; Glocer et al., 2009; Glocer et al 2020). However, major questions remain about the conditions and mechanisms that drive ions, particularly heavy ions that should be gravitationally bound, from thermal energies of ~0.5 eV to escape velocities of a few to 10 eV and ultimately magnetospheric energies of 100 of eV to 100 of keV.

Numerous observations have revealed that plasma of ionospheric origin pervades geospace, and can at times be the dominant source of magnetospheric plasma (Shelley et al 1972; Chappell et al 1987; Haaland et al 2012a; Haaland et al 2012b; Gloeckler and Hamilton 1987). The critical "gate" that controls this vast ionospheric source of plasma—by regulating the mass flux that ultimately escapes to the magnetosphere—is the Exobase Transition Region (ETR). This ETR ranges from just below the exobase (~500 km) to where the ions achieve most of their peak escape flux (≤1,200 km). Within the ETR the ion mean free path becomes longer than the scale height, giving ions a chance to gain enough energy to overcome Earth's gravity. Thus, the ETR is a very important region that must be understood if we are to be able to ultimately understand and predict what controls the fluxes and locations of ionogenic plasma in the magnetosphere.

The ETR hosts two types of ion outflow: light ions (H^+, He^+) propelled upward via the polar wind [Banks and Holzer 1968] and heavier ions such as O^+ that must be heated from above to escape [Roberts et al 1987]. The most episodic and spatiotemporally variable of these flows are the heavy ion outflows, which are predominantly driven in the cusp/cleft region on the dayside, and in the nightside auroral zone.

Measurements throughout this ETR are sorely needed to understand two critical components of this escape process: *ionospheric source*, and *acceleration processes*. The *ionospheric source* consists of cold ions with energies from ~0.5 eV to tens of eV, the transition from gravitationally bound to unbound. This population is one of the least well studied because of the lack of proper measurements. Measurements of evolving cold ion distribution functions are essential to understand ion escape. The *acceleration processes* responsible for ETR ion heating derive their free energy from two major sources: 1) charged particle kinetic energy input, such as magnetospheric electron (e⁻) precipitation, secondary production, and photoelectrons, and 2) electromagnetic energy input, such as magnetospheric Poynting flux, waves, and field-aligned currents.

While many studies have made *in situ* measurements capable of resolving details of ion distribution functions and (synoptically) their variation with altitude within the ETR, as well as many aspects of the energy sources and acceleration mechanisms that may contribute to ion energization and outflow [e.g., Yau et al., 1983; Chaston et al., 2004; Wilson et al., 2004, Lynch et al., 1996; Kintner et al., 1996; Moore et al., 1996], they typically lack the ability to study the spatiotemporal variations of the ion outflow over a finite volume, and to definitively link, on a case by case basis instead of statistically, the energy sources and acceleration mechanisms at work that drive instances of outflow. Studies with ground-based radars [e.g., Søraas et al., 1974, Thayer 1998], can examine many of the bulk properties (flows, densities, temperatures) of the ions and have high spatial and temporal resolution, but are inherently limited in field of view and cannot measure the detailed distribution function of the outflowing ions.

Recognizing the inherently local/one-dimensional nature of single-platform measurement approaches and the need for additional information about ion distribution function variations with altitude and over a larger volume, researchers have turned to energetic neutral atom (ENA) imaging, using the detected ENAs to infer the properties of the accelerated ions. This includes low-altitude low energy ENA imaging from spacecraft (primarily the Swedish microsatellite Astrid) [e.g., C:son Brandt et al., 2000, see also Rowland et al., 2011], or high-altitude low energy ENA imaging from spacecraft, primarily from IMAGE LENA (e.g., Fuselier et al., 2001; Wilson et al., 2003). These approaches demonstrated that it was possible to measure ENAs from low-altitude sources and to examine their spatiotemporal variation and their response to changes in driving.

These pioneering studies were made on fast-moving platforms (satellites), providing little integration time to gather the ENA signal and resolve it spatially (although the Astrid results did resolve low-altitude ENA emissions on regional scales). IMAGE, in particular, was sweeping through perigee quite rapidly, and spinning slowly, when it made its low-altitude measurements. The resulting IMAGE ENA measurements at low altitude show a generally featureless "sea" of low energy ENAs, that would be difficult or impossible to localize with respect to particular auroral features. In fact, a single pixel in the IMAGE reconstruction corresponds to the entire region sampled by VISIONS at much higher spatial resolution.

The VISIONS sounding rocket mission was designed to provide high-spatiotemporal resolution ENA imaging in a local volume (1,000 km × 1,000 km × 1,000 km) with good energy sensitivity, while simultaneously measuring ion distributions, auroral energy inputs (over a wide area), electric and magnetic fields (including wave modes thought to be critical for ion acceleration). With its slow horizontal motion, fast spin rate, and large-aperture ENA detector, as well as a suite of comprehensive and complementary measurements, VISIONS was designed to answer the following science questions:

- What are the spatial and temporal variations of ion outflow in and near an auroral arc?
- What is the total ion outflow in the remotely sensed volume, and what is its variation during the substorm life cycle?
- How do the relative contributions of the energy sources change during the substorm life cycle, and spatially, relative to the visible auroral arcs?
- How do regions of enhanced ion outflow compare in detail to the locations of field-aligned currents, optical auroral emissions, enhanced electric fields, energetic particle precipitation, wave activity, and regions of enhanced/depressed electron density?
- What are the altitudinal locations and extents of ion acceleration regions, and how do these parameters vary over time?

Because the auroral event VISIONS launched into was fairly stable in time (well past substorm onset) we have not been able to determine temporal variations, but the mission was successful in spatially localizing the region where outflow occurred and sheds some light on the relation of ion outflow regions to simultaneously measured auroral input as well as the detailed ion distributions that are associated with the remotely sensed ENAs.

This paper presents an overview of the mission and the initial results from the ENA instrument, showing its ability to spatially localize ion outflow regions at relatively high resolution. Detailed modeling of the ENAs and ion outflow will be presented in a follow-on work.

2 MATERIALS AND METHODS

The VISIONS sounding rocket mission was launched northwards from Poker Flat, AK at 08:21:00.0 UT on 7 Feb 2013, reaching an apogee of 753.8 km 495 s later. The launch occurred approximately 20 mins after the onset of a modest substorm (−400 nT), with breakup north of Poker Flat. The VISIONS rocket trajectory is shown in **Figure 1**. The left panel shows the geographic latitude and longitude of the instrument payload as a function of time in seconds since launch (blue dots). The right panel shows the altitude and latitude of the payload, with labels indicating the position at selected times since launch.
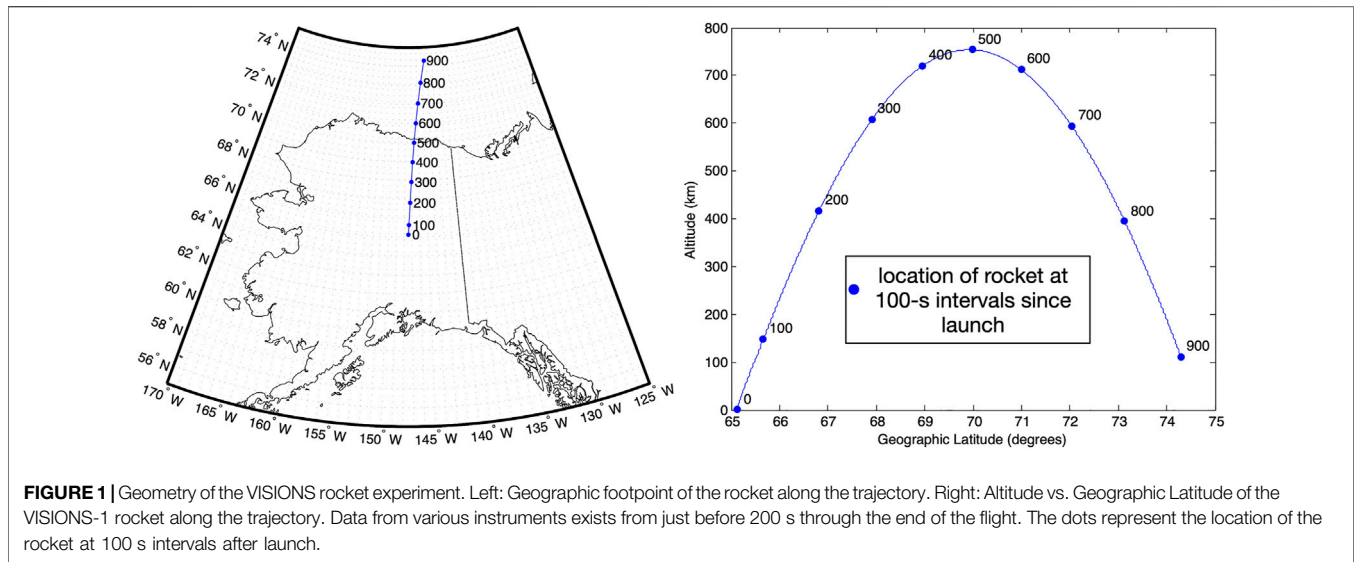
FIGURE 1 | Geometry of the VISIONS rocket experiment. Left: Geographic footpoint of the rocket along the trajectory. Right: Altitude vs. Geographic Latitude of the VISIONS-1 rocket along the trajectory. Data from various instruments exists from just before 200 s through the end of the flight. The dots represent the location of the rocket at 100 s intervals after launch.

TABLE 1 | VISIONS instrument capabilities.

Instrument	Purpose	Capability
MILENA	"Image" low-energy neutral atoms	Six 30° × 5° pixels, 50 eV to 3 keV spin sweeps out "full sky"
RAI	Image visible and near-IR auroral emissions	Nadir-viewing visible light imager with 90° FOV four narrowband wavelengths: 391.4, 630.0, 844.4, 486.1 nm images at 2 Hz rate
EEA	Measure energy-pitch angle distributions of energetic electrons	Energy-pitch angle distributions every 50 ms from 7 eV to 30 keV
EIA	Measure energy-pitch angle distributions of energetic ions	Energy-pitch angle distributions every 50 ms from 3.5 eV to 15 keV
FTP	Measure fields and thermal plasma density and temperature	DC Electric Fields, accuracy 1 mV/m Waves from ULF to 5 MHz Electron density and temperature DC magnetic field, accuracy 2 nT

VISIONS combined remote sensing and *in situ* instruments to provide a new view of ion outflow and its drivers in the nighttime auroral zone, shown in **Table 1**. A brief description of these instruments follows.

2.1 MILENA

The Miniaturized Imager for Low Energy Neutral Atoms (MILENA) is nearly identical to the MINI-ME instrument flown on the FASTSAT mission, launched in 2010 (Rowland et al., 2011). MILENA is essentially a standard top-hat electrostatic analyzer (Carlson, et al., 1983), with an additional front end consisting of a "Venetian blind" set of polished silicon conversion surfaces and an electrostatic charged particle rejector. The charged particle rejector serves to reject energetic electrons and to mechanically collimate the incoming ENAs. The Venetian blind conversion surfaces allow incoming O and H ENAs to capture an electron from the silicon via grazing incidence reflection at fairly high efficiencies (~few %). After electron capture, they become negative ions and are steered through the ESA, first to a microchannel plate, and then to a detector and counter. MILENA uses a "three-bounce" design with

blackened interior surfaces to minimize UV background. VISIONS was launched at night, in moon-down conditions, further reducing the UV signal level that could enter the instrument.

MILENA had an energy range of 50 eV to 3 keV, and a responsivity of approximately 3×10^{-4} counts/s per neutrals/ s-cm^2-sr-dE/E. MILENA's geometric factor was 0.044 sr, corresponding to a solid angle of 31.9 × 4.5° and an aperture of 4 cm^2. MILENA's energy resolution (dE/E) was 20%. MILENA's integration period was 16 ms, with 128 integrations per energy step (the total duration of each energy step was 2.048 s). The VISIONS rocket was kept nearly aligned to the background magnetic field (within about 8°) and spun at a rate of ~0.48 Hz.

VISIONS flew two identical MILENA instruments, M1 and M2. M1 stepped over the following eight energies: 50, 70, 100, 300, 500, 700, 1,000, and 3,000 eV, changing energies every 2.048 s. M2 alternated between 50 and 100 eV every 2.048 s. The instrument aperture plane contained the spin axis of the rocket, and so each imager swept out a "full sky" image every half-spin, or approximately once per second. The MILENA sectors

each had an angular extent of ~30° in polar angle (in the aperture plane), and there were six per instrument, with ~30° gaps between sectors. The angular acceptance in the azimuthal direction (perpendicular to the aperture plane) was approximately ±2.25°. Sectors 1 and 2 look downward, with sector centers at 30° from the rocket spin axis (which is aligned roughly to the magnetic field direction) and are the sectors closest to "nadir"). Sectors 3 and 6 look horizontally, with centers at 90° to the rocket spin axis. Sectors 4 and 5 look upward with centers at 30° from the rocket spin axis (opposite the magnetic field direction, these are the sectors closest to viewing in the zenith). Collier et al., 2015 highlights some initial measurements from VISIONS-1 MILENA.

2.2 RAI

The Rocket-borne Auroral Imager (RAI) consisted of four independent narrowband visible-light imagers, each tuned to a unique wavelength (Hecht et al., 2006). Each had an identical 90° wide field of view, achieved using telecentric optics that are consistent with the narrowband interference filters used. After onboard binning, the resulting images were captured twice per second at 128 × 128 pixel resolution. The instrument sensitivity was a few 100 Rayleighs in all four channels. The four wavelengths selected were 1) 391.4 nm, to measure energetic electron precipitation, 2) 630.0 nm, to measure softer electron precipitation, 3) 844.4 nm, to provide another measure of atomic oxygen density, and 4) 486.1 nm, H-beta, to look for proton precipitation and regions of albedo ENA production. These lines were selected to permit an estimation of electron energy flux and characteristic electron energy in each pixel, using the technique of Hecht et al. (2006). When the rocket was near apogee (~750 km), the RAI pixel size was approximately 10 km, assuming a projection height of 100 km. RAI was deployed on a sub-payload which was three-axis stabilized, to avoid motion or spin-blur effects on the image. The RAI apertures were kept pointing near the 100 km altitude point above Arctic Village, Alaska, with three updates to the pointing throughout the flight, to stay near this target.

2.3 EEA and EIA

The Energetic Electron Analyzer (EEA) and Energetic Ion Analyzer (EIA) [Clemmons et al., 2013] were top-hat electrostatic analyzers (Carlson et al., 1983) for measuring electrons and ions, respectively. These instruments had instrument aperture planes that contained the spin plane of the rocket. Since this rocket spin axis was kept nearly aligned to the magnetic field, this geometry permitted full pitch angle distribution measurements. The instruments each utilized twenty pixels of various sizes ranging from 3° (near 90° pitch angle on EIA to sample transverse ions, and near 0° pitch angle on EEA to sample precipitating electrons) to 12°. The instruments each had a geometric factor of 0.01 cm^2-s-sr keV/keV, energy resolution of 16%, and integration times of 1 ms per energy step. They swept over 50 energies in a total energy sweep time of 50 ms. EIA measured ions from 7.5 eV to 15 keV. EEA measured electrons from 15 eV to 30 keV. These instruments also mapped out a full three-dimensional distribution every half spin (approximately once per second).
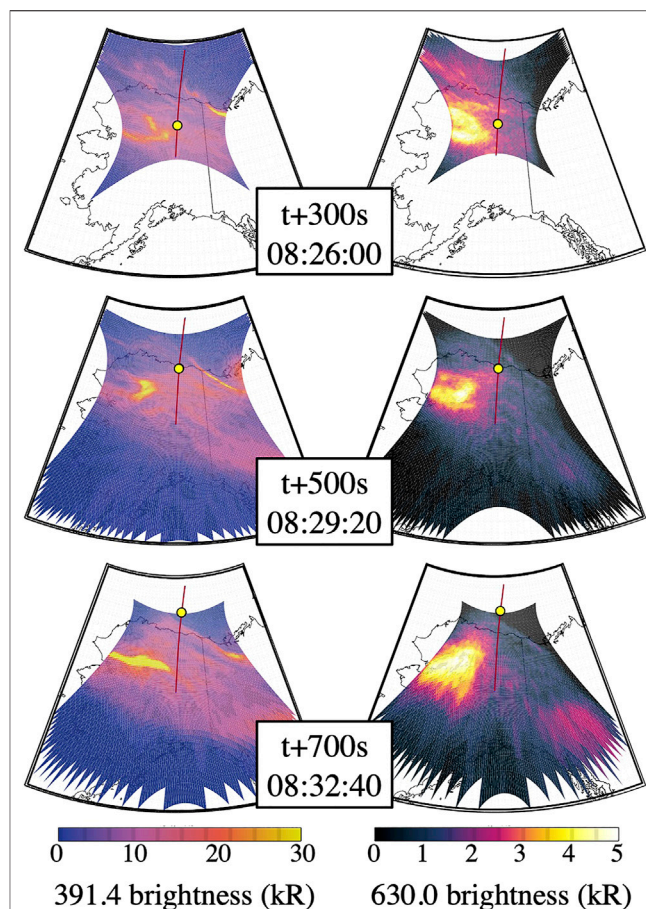
FIGURE 2 | Representative auroral images during VISIONS flight, with rocket trajectory (red line) superimposed. The yellow dot indicates the payload position at the time of the given auroral image. Each row represents the 391.4 emissions (left) and 630.0 nm emissions (right) measured onboard the VISIONS rocket by the nadir-viewing Rocket Auroral Imager (RAI), projected onto a geographic reference altitude of 120 km (391.4) or 200 km (630.0). Each column shows a separate time point during the flight ranging from t + 300 s since launch (top row) to t + 700 s since launch (bottom row). The important feature of this plot is that there is a large and persistent 630.0 nm emission feature to the west/southwest of the rocket trajectory, and bright 391.4 nm emissions from both the southwest and northeast of the trajectory, and these features persist throughout the entire rocket flight.

2.4 FTP

The Fields and Thermal Plasma instrument suite (FTP) consisted of a vector double-probe electric field instrument, a cylindrical Langmuir Probe, a dipole impedance probe, and a fluxgate magnetometer on the main payload and a single axis wave electric field double probe, magnetometer, and Langmuir probe on the sub-payload. For the purposes of this study, we focus on the fields and thermal plasma instruments on the main payload.

The double-probe instrument measured the electric field from quasi-static (DC) frequencies to 5 MHz perpendicular to the background magnetic field, along which the payload spin axis was oriented by the on-board attitude control system. Four spherical electric field sensors with embedded pre-amps were

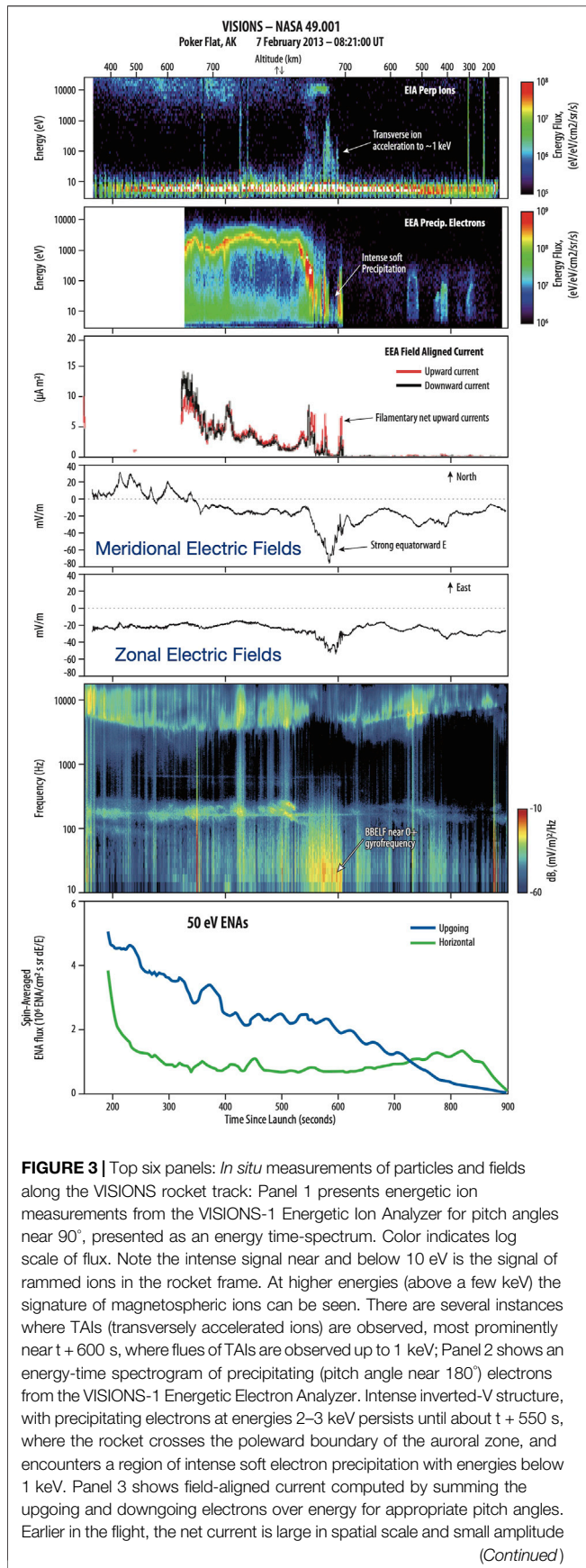**FIGURE 3 |** Top six panels: *In situ* measurements of particles and fields along the VISIONS rocket track: Panel 1 presents energetic ion measurements from the VISIONS-1 Energetic Ion Analyzer for pitch angles near 90°, presented as an energy time-spectrum. Color indicates log scale of flux. Note the intense signal near and below 10 eV is the signal of rammed ions in the rocket frame. At higher energies (above a few keV) the signature of magnetospheric ions can be seen. There are several instances where TAIs (transversely accelerated ions) are observed, most prominently near t + 600 s, where fluxes of TAIs are observed up to 1 keV; Panel 2 shows an energy-time spectrogram of precipitating (pitch angle near 180°) electrons from the VISIONS-1 Energetic Electron Analyzer. Intense inverted-V structure, with precipitating electrons at energies 2–3 keV persists until about t + 550 s, where the rocket crosses the poleward boundary of the auroral zone, and encounters a region of intense soft electron precipitation with energies below 1 keV. Panel 3 shows field-aligned current computed by summing the upgoing and downgoing electrons over energy for appropriate pitch angles. Earlier in the flight, the net current is large in spatial scale and small amplitude *(Continued)*

FIGURE 3 | or slightly downward, while in the region of soft electron precipitation the current is upgoing, stronger, and highly filamentary. Panels 4 and 5 show the meridional and zonal components of the electric field (in magnetic coordinates) measured by the double probe electric field experiment on VISIONS-1, showing an intense equatorward electric field in the region of soft precipitation and filamentary upward current, that exhibits the TAI signature. Panel 6 shows a Fourier spectrogram of the ELF/VLF electric field wave environment. Intense lower hybrid emissions with a sharp cutoff can be seen at the top of the figure, with an enhancement of broad-band ELF (BBELF) waves that span the O+ gyrofrequency in the region where TAIs are observed. Bottom panel: Spin-averaged (2 s average) fluxes of 50 eV energetic neutral atoms (ENAs) from one of the MILENA imagers. The blue trace indicates ENAs that are coming from primarily below the rocket (dominant before about 700 s), while the green are ENAs coming from primarily horizontal angles of arrival. The angle of arrival is measured using six angular sectors of 30° width with 30°-wide gaps between them.

deployed at the end of 3 m long "stacer" booms to form orthogonal 6 m tip-to-tip double probes in the spin plane. The electric field measurement was gathered continuously over a range of frequency bands, including: 1) "DC-coupled" channels with a sample rate of 2 kHz and a range of ±833 mV/m at 18-bit precision and an absolute accuracy of approximately 0.5 mV/m, 2) "AC-coupled" VLF channels with a high pass filter at 16 Hz that were sampled at 32 kHz at 18 bits, for which the most significant 15 bits were telemetered to the ground, over a range of ±45.7 mV/m, and 3) HF electric fields sampled at 5 Ms/s with a 12 bit analog-digital converter. The cylindrical Langmuir Probe was designed to measure the thermal electron density and temperature (during sweeps of the bias voltage) as well as small-scale variations in the ion density (during intervals when the probe was held at a negative bias voltage). It was sampled at 8 kHz, and the voltage sweep ran from −2 to +3 V over 256 ms, once every 10 seconds. The impedance probe measured the impedance of a short dipole antenna exposed to the plasma, from which observed resonances were used to measure the upper hybrid frequency and thus the electron number density (see, e.g., Jensen and Baker, 1992), approximately six times per second. The fluxgate magnetometer was a three-axis Bartington MAG-03MSB60, sampled at 18 bits at 2 kHz per channel. The absolute accuracy was approximately 2 nT.

3 RESULTS

3.1 RAI Auroral Images

Figure 2 shows the rocket trajectory superimposed on a set of representative images from the RAI instrument. In each column is shown a different wavelength, with 391.4 nm on the left and 630.0 nm on the right. Time increases down each column, and the three pairs of images span more than 6.5 min of the flight. The rocket trajectory is shown as a thin blue line, with a yellow dot indicating the payload position at the given time. The 391.4 nm image is projected to 120 km altitude, while the 630.0 nm image is projected to 200 km altitude. All images have undergone dark current subtraction and 3 × 3 median filtering from the original 128 × 128 pixel images.

The images show that VISIONS passed to the east of a large, stable region of intense precipitation, both hard (391.4) and soft (630.0), and to the west of a more dynamic feature that is more readily apparent in 391.4. The complete sequence of auroral images (not shown here) indicates that a dynamic set of arcs was forming and evolving near the polar cap boundary, including the poleward arc encountered by VISIONS. In addition, a combination of ground-based whitelight imagers and the full image sequence from VISIONS showed that the strong auroral feature to the west of the rocket trajectory is stable throughout the flight and for ~10 min before and >30 min after. Some of the apparent variation in the emissions (particularly in the 630.0 nm line, in the later portion of the flight is due to the changing viewing angle relative to the magnetic field and projection effects. See **Figure 5** for similar ground-based images of the persistence of the auroral features.

3.2 *In situ* Measurements of Particles and Fields

The *in situ* measurements from the VISIONS flight are shown in **Figure 3**. VISIONS was launched into a region of inverted-V electron precipitation (~2–3 keV electrons), as shown in the second panel. The inverted-V electron precipitation transitioned to a region of intense soft electron precipitation at the polar cap boundary, between about 500 and 600 s after launch (just after apogee), with electron energies at or below a few 100 eV. The polar cap boundary also exhibited signatures of transversely accelerated ions (panel 1), with energies up to 1 keV, coincident with the soft precipitation. This region also exhibited intense, filamentary field aligned currents (panel 3, net upward current of ~5–10 μA/m^2) as measured by the energetic particle instrument, strong equatorward DC electric fields (~90 mV/m, panel 4 and 5), and intense BBELF waves near the O+ gyrofrequency which was near 40 Hz at this location (panel 6). These intense filamentary upward currents may be capable of exciting O+ ion cyclotron waves in the range 400–1,000 km, depending on the details of the Te/Ti ratio and ion composition profiles, which were not directly measured by VISIONS (Kindel and Kennel, 1971). These are fairly typical signatures of the nightside auroral zone following a substorm [see, e.g., Lynch et al., 1996] and have been discussed further in a companion paper (Clemmons, 2014).

Taken together, these figures show that VISIONS flew through some regions with transversely accelerated ions and active aurora but did not encounter the regions of most intense auroral precipitation (or, presumably, ion acceleration). Throughout most of the flight, the largest, most intense region of precipitation was to the southwest of the rocket, with narrow arcs of harder precipitation at the polar cap and to the east.

3.3 ENA Measurements

To understand how these more distant regions of auroral precipitation might have driven ion energization, it is instructive to examine the ENA emissions observed by VISIONS. The ENAs, as described above, are generated as energetic ions charge exchange with the neutral atmosphere.

These ENAs can be remotely observed at large distances from the parent ion population. The ENA fluxes can thus serve as proxies for the line of sight-integrated ion populations.
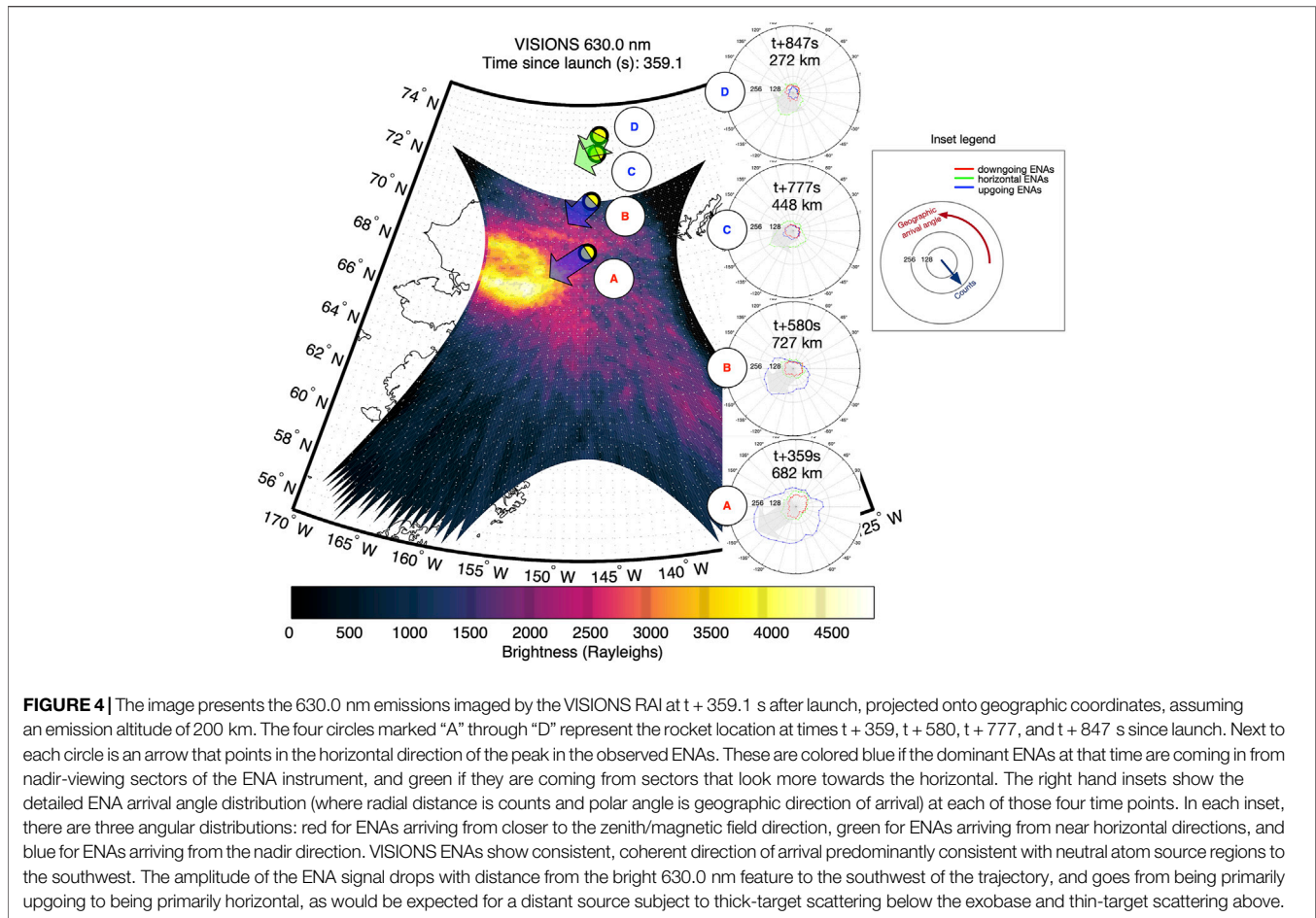
3.3.1 Spin-Averaged ENA Data

Panel 7 of **Figure 3** shows data from MILENA. In this case, the data shown are the 50 eV channel data from MILENA's M2 sensor, summed over a full 2-s energy step (nearly the same as the spin period) for two pairs of the six arrival angle sectors. The blue traces are for ENAs traveling within ±45° of the direction opposite to the magnetic field (up the field line). The green traces correspond to "horizontal" ENAs traveling within ±15° of the direction perpendicular to the magnetic field. The horizontal axis of the plot shows time since launch. The vertical axis represents the ENA number flux in a given pixel. The integration time was 2.048 s.

As the rocket ascends, in the early part of the flight before apogee (in the auroral zone, inverted-V region) the upgoing ENAs dominate over the horizontal and downgoing ENAs. The upgoing ENAs also diminish in intensity with time, presumably as the rocket moves farther away from the source region in distance, and potentially also reflecting the angular distribution of upgoing ENAs, reducing significantly out in the polar cap. The downgoing ENAs (not shown) are generally weak throughout the flight. The horizontal ENAs start out at high levels, as the rocket is near peak ENA production altitudes and also closest to the source in the early part of the flight, then remain stable and low once the rocket has reached higher altitudes where horizontal ENA production is lower, and then go on to increase when the rocket is on the descending portion of its trajectory in the polar cap, even though the rocket is farther from the source at this point. Indeed, the horizontal ENAs become dominant just after t + 800 s.

3.3.2 Angle-Resolved ENA Data

While the spin-averaged data is valuable and provides some important clues about the nature and sources of ENA production, it is the sub-spin "ENA imaging" data from MILENA that shows the promise of this technique. **Figure 4** shows four panels of subspin data (inset polar plots) from M2 50 eV data at each of four different times during the VISIONS flight: 1) t + 359 s, in the auroral zone, at 682 km; 2) t + 580 s near the polar cap boundary, at 727 km altitude; 3) t + 777 s, at 428 km altitude, in the polar cap; and 4) t + 847 s, 242 km altitude, below the exobase in the polar cap. In each panel, the combined count rate from each pair of matched pixels is shown as a function of arrival direction, using the same color scheme as **Figure 3**, with the addition of red traces showing downgoing ENAs (±45 of the direction of the magnetic field). North is to the top of each panel, and east to the right. The angle shown is the projection of that pixel's center look direction onto a horizontal plane as a function of time. The radial distance of each curve from the center of the panel indicates the counts measured by M2 at that angular location. For each panel, an arrow (blue for auroral zone, green for polar cap) is superimposed on the point on the rocket trajectory corresponding to that observation. Also superimposed is the RAI 630.0 nm image from t + 359 s, for

FIGURE 4 | The image presents the 630.0 nm emissions imaged by the VISIONS RAI at t + 359.1 s after launch, projected onto geographic coordinates, assuming an emission altitude of 200 km. The four circles marked "A" through "D" represent the rocket location at times t + 359, t + 580, t + 777, and t + 847 s since launch. Next to each circle is an arrow that points in the horizontal direction of the peak in the observed ENAs. These are colored blue if the dominant ENAs at that time are coming in from nadir-viewing sectors of the ENA instrument, and green if they are coming from sectors that look more towards the horizontal. The right hand insets show the detailed ENA arrival angle distribution (where radial distance is counts and polar angle is geographic direction of arrival) at each of those four time points. In each inset, there are three angular distributions: red for ENAs arriving from closer to the zenith/magnetic field direction, green for ENAs arriving from near horizontal directions, and blue for ENAs arriving from the nadir direction. VISIONS ENAs show consistent, coherent direction of arrival predominantly consistent with neutral atom source regions to the southwest. The amplitude of the ENA signal drops with distance from the bright 630.0 nm feature to the southwest of the trajectory, and goes from being primarily upgoing to being primarily horizontal, as would be expected for a distant source subject to thick-target scattering below the exobase and thin-target scattering above.

comparison and to show a representative distribution of auroral emissions. While these change slightly with time, the main feature (large emission region to the southwest of the rocket) does not vary significantly through the VISIONS flight. While there is some variation in the ENA arrival direction with time as the rocket moves along its trajectory, it is clear that the strongest signals are to the southwest of the rocket. The data are consistent with multiple weaker sources at other angular positions as well, in some cases. The transition from upgoing ENAs in the top two panels to horizontal ENAs in the bottom (lower altitude, polar cap) panels is quite clear.
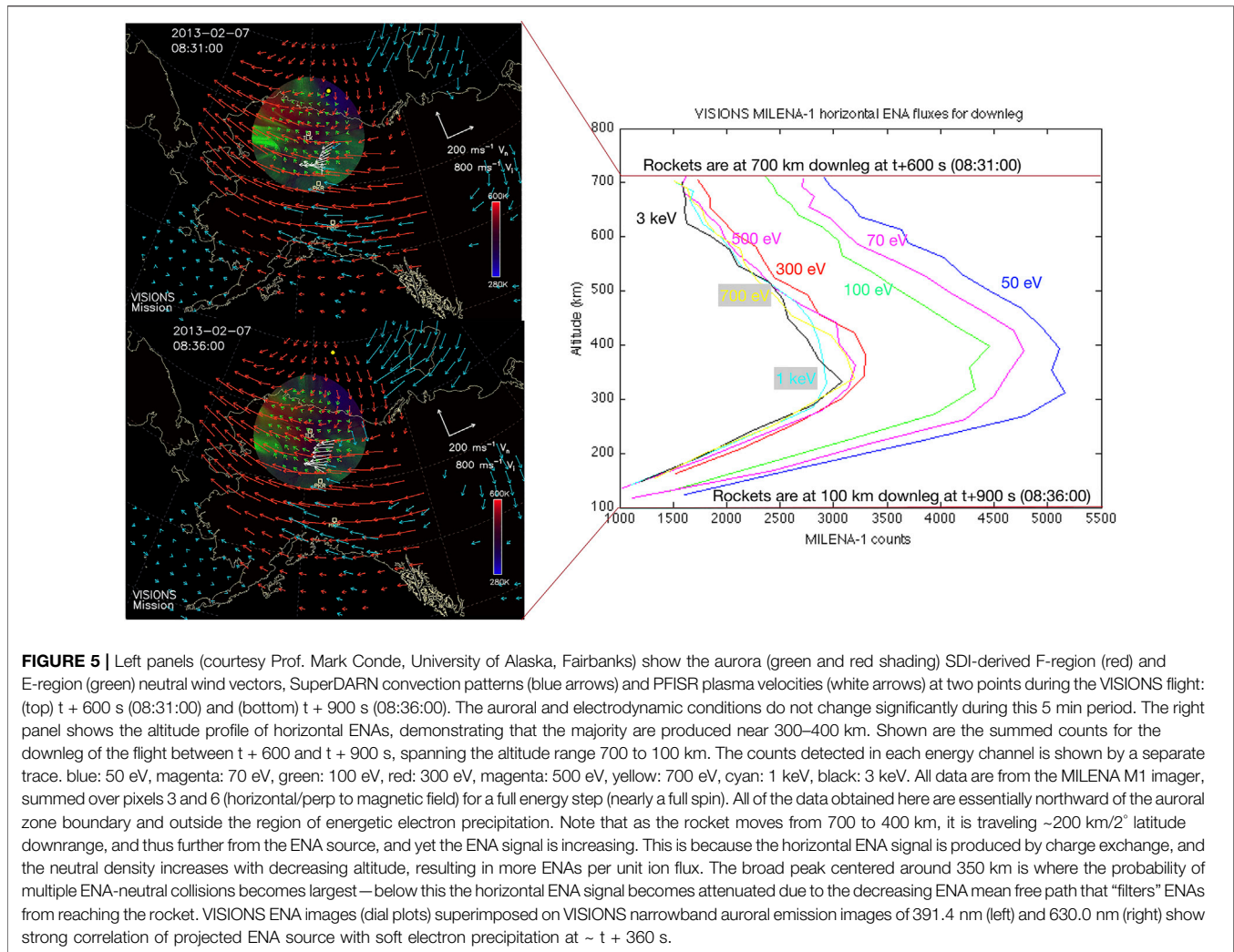
In order to spatially localize the region of outflow, it is important to assess which magnetic flux tubes are associated with regions of outflow and how these outflow regions relate to regions of energy inputs, particularly auroral inputs. In so doing, we can collapse the (important) altitude dependence to answer the question—to first order, where are the ENAs coming from? This will be important both to address the VISIONS science questions and to develop improved techniques for reconstructing accelerated ion populations from ENA measurements in optically thick regions.

The usual technique for analyzing ENA data [see, e.g., Roelof, 1987 or Roelof and Skinner, 2000] assumes an optically thin medium, and takes the line integral of the product of the neutral atom density and ion flux along the line of sight, times the charge exchange cross section. Observations of this ENA source function along different lines of sight are used to tomographically reconstruct the ion population (or simulated ENA images are generated, compared with observations, and iterated until a match is achieved, see also Fok et al., 2003 and Wilson et al., 2003). As discussed in Roelof (1997), low-altitude ENA imaging must deal with the complications of an optically thick medium, including attenuation, scattering, re-ionization, and reverse charge exchange. For the VISIONS regime, near the exobase, the optically thin approximation is not strictly valid. A "thick target" approach, similar to that used by Bazell et al. (2010) would be a more rigorous approach, in terms of accounting for multiple scattering, charge exchange, stripping, and other effects.

3.3.3 Altitude Variations in ENA Production and "Thin Shell" Backtracing
However, to first order, since VISIONS is relatively close to the source, we can approximate the ENA source region as optically thin above about 400 km (where the mean free path for ENA-neutral collisions becomes >100 km, assuming no collisions in this optically thin region [see, e.g., C:son Brandt
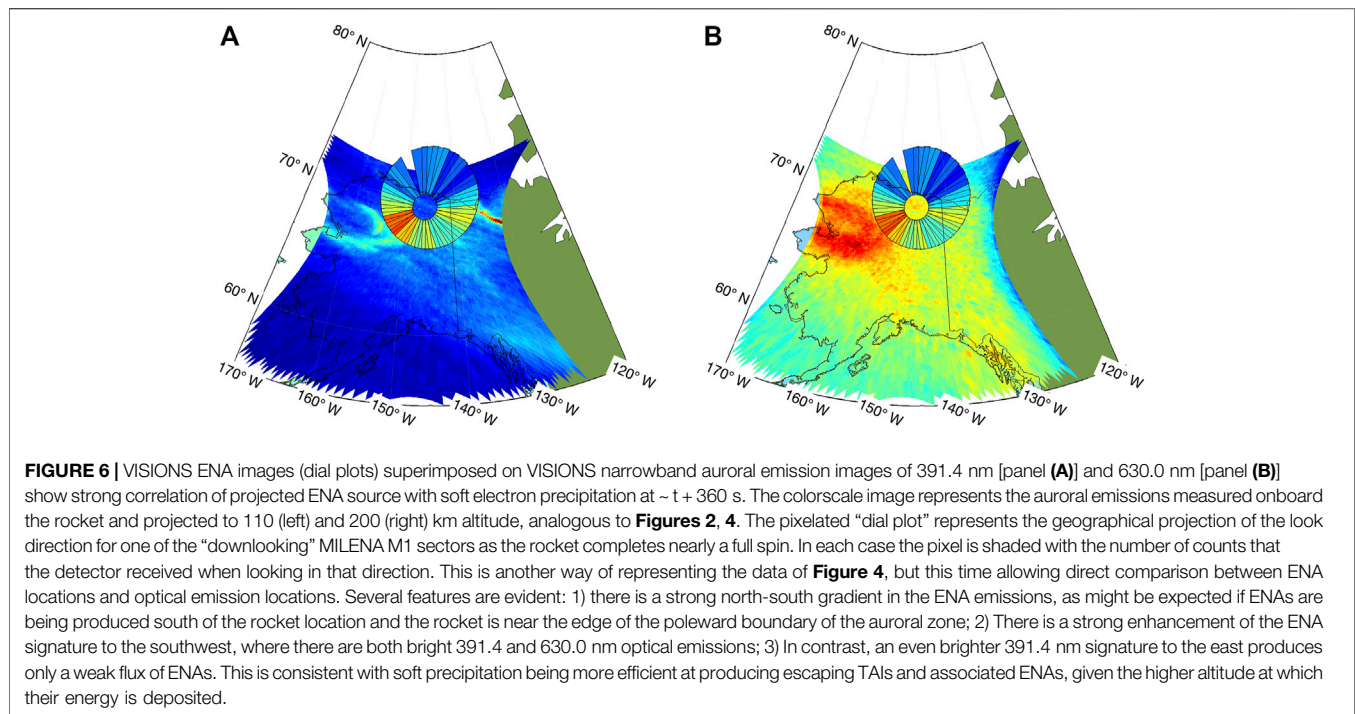
FIGURE 5 | Left panels (courtesy Prof. Mark Conde, University of Alaska, Fairbanks) show the aurora (green and red shading) SDI-derived F-region (red) and E-region (green) neutral wind vectors, SuperDARN convection patterns (blue arrows) and PFISR plasma velocities (white arrows) at two points during the VISIONS flight: (top) t + 600 s (08:31:00) and (bottom) t + 900 s (08:36:00). The auroral and electrodynamic conditions do not change significantly during this 5 min period. The right panel shows the altitude profile of horizontal ENAs, demonstrating that the majority are produced near 300–400 km. Shown are the summed counts for the downleg of the flight between t + 600 and t + 900 s, spanning the altitude range 700 to 100 km. The counts detected in each energy channel is shown by a separate trace. blue: 50 eV, magenta: 70 eV, green: 100 eV, red: 300 eV, magenta: 500 eV, yellow: 700 eV, cyan: 1 keV, black: 3 keV. All data are from the MILENA M1 imager, summed over pixels 3 and 6 (horizontal/perp to magnetic field) for a full energy step (nearly a full spin). All of the data obtained here are essentially northward of the auroral zone boundary and outside the region of energetic electron precipitation. Note that as the rocket moves from 700 to 400 km, it is traveling ~200 km/2° latitude downrange, and thus further from the ENA source, and yet the ENA signal is increasing. This is because the horizontal ENA signal is produced by charge exchange, and the neutral density increases with decreasing altitude, resulting in more ENAs per unit ion flux. The broad peak centered around 350 km is where the probability of multiple ENA-neutral collisions becomes largest—below this the horizontal ENA signal becomes attenuated due to the decreasing ENA mean free path that "filters" ENAs from reaching the rocket. VISIONS ENA images (dial plots) superimposed on VISIONS narrowband auroral emission images of 391.4 nm (left) and 630.0 nm (right) show strong correlation of projected ENA source with soft electron precipitation at ~ t + 360 s.

et al., (2001)]. We refer to this as a "thin shell" backtracing approach. Even though the ENAs are generated over a range of altitudes and ranges along the instrument's line of sight, we assume all ENAs originate from the boundary where the atmosphere becomes optically thick. Below about 400 km this condition is satisfied with mean free paths approaching 10 km near 300 km altitude. It is important to note that the point at which the ENA leaves the optically thick medium is not, in general, the same as where the original parent ion underwent charge exchange, as there can be a great deal of ENA-neutral scattering in this optically thick region, resulting in spatial smearing of features. This scattering also tends to degrade information on the initial parent ion's energy and pitch angle, which get heavily smeared by scattering in this layer. ENAs produced by charge exchange in the optically thin region (typically horizontally traveling ENAs) do not have this problem to the same extent.

To assess the validity of this "thin shell" approach, we examined the altitude dependence of the horizontal ENAs observed by VISIONS as it flew through the descending portion of its trajectory in the polar cap. **Figure 5** shows the

sum of M1 pixels 3 and 6 (sidelooking pixels, perpendicular to magnetic field ± 15°) as a function of altitude for each of the eight M1 energy steps, summed over pixels 3 and 6 for each 2.048 s energy step (nearly a full spin). The energy spectrum is fairly constant with altitude, and is roughly consistent with a power law of slope −0.3, becoming harder at altitudes below 300 km, consistent with more energetic ENAs being able to reach the spacecraft when lower energy ENAs have their energy degraded and their flux attenuated by ENA-neutral collisions.

These data are plotted as a function of altitude, but the rocket is also moving northwards, during this interval (about 300 km northwards while the rocket descends from 700 to 300 km altitude). In addition, the charge exchange probability increases with decreasing altitude, an effect that is not corrected for here. Finally, the detailed ion population pitch angle, energy, and altitude distribution is not known over the entire ENA source region and can be expected to be variable in space and time over the energy input region. The left panels of **Figure 5** show the relative stability of the auroral and electrodynamic conditions during the 5 min period that corresponds to the rocket downleg descent from 700 to

FIGURE 6 | VISIONS ENA images (dial plots) superimposed on VISIONS narrowband auroral emission images of 391.4 nm [panel **(A)**] and 630.0 nm [panel **(B)**] show strong correlation of projected ENA source with soft electron precipitation at ~ t + 360 s. The colorscale image represents the auroral emissions measured onboard the rocket and projected to 110 (left) and 200 (right) km altitude, analogous to **Figures 2**, **4**. The pixelated "dial plot" represents the geographical projection of the look direction for one of the "downlooking" MILENA M1 sectors as the rocket completes nearly a full spin. In each case the pixel is shaded with the number of counts that the detector received when looking in that direction. This is another way of representing the data of **Figure 4**, but this time allowing direct comparison between ENA locations and optical emission locations. Several features are evident: 1) there is a strong north-south gradient in the ENA emissions, as might be expected if ENAs are being produced south of the rocket location and the rocket is near the edge of the poleward boundary of the auroral zone; 2) There is a strong enhancement of the ENA signature to the southwest, where there are both bright 391.4 and 630.0 nm optical emissions; 3) In contrast, an even brighter 391.4 nm signature to the east produces only a weak flux of ENAs. This is consistent with soft precipitation being more efficient at producing escaping TAIs and associated ENAs, given the higher altitude at which their energy is deposited.

100 km. With all these issues in mind, this figure does show that the horizontal ENAs observed by VISIONS peak in the 300–400 km altitude range, consistent with our thin shell tracing to first order.

For an initial analysis, we thus assume that the upgoing ENAs observed by VISIONS come from a thin shell at 375 km. While the data in **Figure 5** show a range in altitudes where peak ENAs are observed, small differences in the assumed "thin shell" altitude do not substantially alter the backtracing, given the inherently low resolution of the ENA imager and the significant effects of ENA-neutral scattering. We backtrace the ENAs using straight-line trajectories (valid for energies significantly above escape velocity) and locate the point at which that backtraced trajectory intersects a 375 km altitude spherical surface.
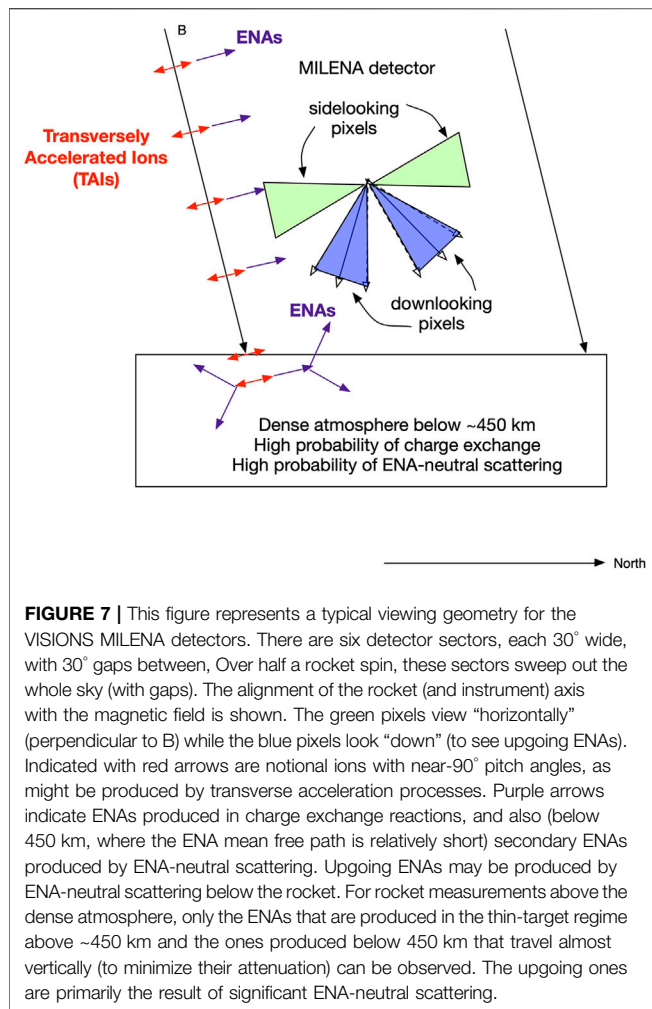
The result is shown for a particular time in the flight (t + 360 s) in **Figure 6**. It is important to note that we do not have directly measured ion distributions on the flux tubes where the highest ENA counts seem to be coming from. The RAI images from **Figure 2** are shown again, with 391.4 nm on the left, and 630.0 nm on the right. Superimposed on these is a "dial plot" showing the projections of the M2 pixel "1" count rates onto the 375 km spherical surface. Color is used to indicate the count rate in each spin sector. The dial plots in the two panels are identical—they are repeated for clarity. In both panels, the strongest ENA emissions show a strong overlap with the region of strong auroral emissions (especially 630.0 nm) to the southwest of the rocket. There is also a slight enhancement in the ENA count rate associated with the narrow but intense 391.4 emissions to the east of the rocket. The asymmetric shape of the ENA pixels when

projected to the reference altitude result from the fact that the payload is aligned near the magnetic field, which has a finite inclination.

4 DISCUSSION

The only other low energy (<1 keV) ENA observations near the nighttime auroral zone below 1,000 km come from the IMAGE LENA instrument (Moore et al., 2000), the PIPPI instrument on Astrid (Barabash et al., 1997), and the MINI-ME instrument on FASTSAT (Rowland et al., 2011). IMAGE LENA saw an omnipresent source of low energy ENAs of broad angular extent, including some that were coming from the nadir (Wilson et al., 2004). LENA did not have energy discrimination capability, and may have been susceptible to angular scattering of the rammed signal which tends to broaden the observed ENA signal. This featureless "sea" of low energy ENAs was also likely dominated by proton precipitation and dayside ENA emissions, since there were few IMAGE perigee passes during or immediately following an auroral substorm. PIPPI saw structured ENAs between 0.1 and 13 keV, with ENA "pitch angles" between 110° and 140° [C:son Brandt et al., 2001]. These emissions were at latitudes above the auroral zone, however. At higher altitudes, missions such as TWINS have seen higher energy (2 keV to tens of keV) "low altitude emissions" or LAEs [Bazell et al., 2010] coming from predominantly "ENA albedo" or backsplash from precipitating magnetospheric protons [e.g., Torr et al. (1974); Kozyra et al. (1982)]. These emissions have been observed primarily at near-horizontal ENA pitch angles, due to the required observing geometry.

Three main aspects of the VISIONS results are new and warrant further examination: 1) the predominance of upgoing

FIGURE 7 | This figure represents a typical viewing geometry for the VISIONS MILENA detectors. There are six detector sectors, each 30° wide, with 30° gaps between, Over half a rocket spin, these sectors sweep out the whole sky (with gaps). The alignment of the rocket (and instrument) axis with the magnetic field is shown. The green pixels view "horizontally" (perpendicular to B) while the blue pixels look "down" (to see upgoing ENAs). Indicated with red arrows are notional ions with near-90° pitch angles, as might be produced by transverse acceleration processes. Purple arrows indicate ENAs produced in charge exchange reactions, and also (below 450 km, where the ENA mean free path is relatively short) secondary ENAs produced by ENA-neutral scattering. Upgoing ENAs may be produced by ENA-neutral scattering below the rocket. For rocket measurements above the dense atmosphere, only the ENAs that are produced in the thin-target regime above ~450 km and the ones produced below 450 km that travel almost vertically (to minimize their attenuation) can be observed. The upgoing ones are primarily the result of significant ENA-neutral scattering.

ENAs in the auroral zone; 2) the altitudinal dependence of the ENAs in the polar cap; and 3) the spatial localization of the ENA emissions and its strong association with 630.0 nm auroral emissions.

4.1 Upgoing ENAs

Since the charge-exchange reaction is nearly conservative in momentum and energy, upgoing ENAs could be produced by upgoing ions with pitch angles near 180°. Since the upgoing ENAs observed by VISIONS are at energies of 50 eV and higher, this would require an energization mechanism active below 400 km (the lowest altitude on the upleg where we have MILENA data) that could energize ions to 50 eV with pitch angles >135°. Previous observations of TAIs [e.g., Kintner et al., 1996; Lynch et al., 1996] at low altitudes show distributions that are much more strongly peaked near 90°. In principle, a very strong energization mechanism could produce a significant upgoing ENA flux that was itself a small fraction of the 90° energization, with the low-altitude 90° ENAs not observable due to the experiment geometry and/or attenuation in the neutral atmosphere. We do not deem this explanation likely to be able to explain the VISIONS results.

The other explanations for strong fluxes of upgoing ENAs all involve ENA-neutral scattering. In these scenarios, a near-90° TAI (transversely accelerated ion) undergoes charge exchange, resulting in a near-90° "pitch angle" ENA. For this to result in a strong upgoing ENA flux, this ENA must scatter off of a cold neutral atom (or undergo multiple scattering) in the thermosphere. **Figure 7** shows the basic geometry, with magnetic field lines indicated in black, energetic ions schematically shown as red arrows, and purple arrows indicating ENAs. The rectangle at the bottom of the figure shows schematically the atmosphere below 400 km, which is "optically thick" and in which ENA-neutral scattering is likely. Four of the six MILENA pixels are also shown, for reference.

There are at least five ways in which this can happen: 1) local ENA-neutral scattering in the "optically thin" region above 400 km; 2) backscatter of "near 90°" ENAs that happen to have downward vertical velocities due to the magnetic declination; 3) albedo ENA generation from precipitating multi-keV ions (either plasma sheet ions or conjugate transversely accelerated/outflowing ions from the other hemisphere); 4) low altitude acceleration—when the TAIs are formed below 400 km when the mean free path is short; or 5) a "pressure cooker" scenario after Gorney et al., 1985.

In the local scattering scenario, the "near-90° pitch angle" ENA scatters off a cold neutral atom at high altitude (above 400 km), and then sometimes travels upwards where it can be detected by MILENA. This scenario is not very consistent with the fact that mean free paths above 400 km are on the order of 100 km or longer. There would have to be incredibly intense ion fluxes to produce the observed ENA fluxes in this scenario.

In the backscatter scenario, there will be a population of "downward" ENAs traveling down to the exobase, for certain gyrophases of the parent ion at the moment of charge exchange. Due to the finite magnetic declination (nearly 16° for VISIONS), "90° pitch angle" ENAs may have a range of vertical velocity angles relative to zenith/nadir, corresponding to ± 16° depending on the parent ion gyrophase. Some fraction of the ENAs thus produced will travel vertically downward (although at a shallow angle) and may then scatter off the dense atmosphere below the parent ion population. Some fraction of those scattered ENAs may then backscatter upwards, to be viewed by the VISIONS MILENA instrument. Due to the small declination, we would expect ENAs to preferentially be generated south of auroral features, and separated at some distance (a few 100 km away). Initial indications are that the northern edge of the auroral feature lines up well with the northern edge of the ENA emissions, but this will require more detailed analysis to rule out.

In the albedo ENA scenario (Roelof 1997) the precipitating energetic ions (6–8 keV) shown in **Figure 3** would generate ENAs as they (mostly) charge exchange near the exobase. The VISIONS *in situ* instruments recorded these multi-keV ions throughout the flight, with an intensification both in energy and flux right at the polar cap boundary in the region of transversely accelerated ions. We have no direct measurements regarding their presence or fluxes away from the rocket trajectory, but the H-β channel of the RAI (which was designed to measure emissions associated with proton precipitation—see, e.g., Søraas et al. [1996], Synnes et al.

FIGURE 8 | This figure presents three scenarios for ENA production. In each case, the gray shaded region represents the dense neutral atmosphere below the exobase, where the ENA mean free path becomes short compared to the atmospheric scale height. The shaded red boxes are meant to indicate a notional altitude region where significant transverse ion acceleration is ongoing, and the helical symbols and blue arrows represent transverse ions and primary and secondary ENAs. The three panels show: **(A)** high altitude acceleration that does not extend into the dense atmosphere produces primarily horizontal ENAs as the mirror force pushes accelerated ions out. To the extent that the acceleration produces ions with slightly downgoing (but near 90) pitch angles, those ions will reach the dense atmosphere and can produce upgoing ENAs. **(B)** if the acceleration region extends to low-altitude, the acceleration produces mainly upgoing ENAs, and **(C)** High altitude parallel electric field pressure cooker reflects ions back down to the exobase, amplifying the weak upgoing signal from scenario "A".

[1998]) saw very low emissions during the flight (down to the sensitivity of the imager, channel, about 200 R) when the RAI was pointed to the nadir. At the end of the flight, the RAI viewed the limb, and limb brightening raised the H-beta signal to ~0.5 erg/cm^2/s on average, with a slightly brighter emission of ~1 erg/cm^2/s to the southwest, in a similar direction to the region of ENA production and strong 630.0 nm emission. In contrast, the electron fluxes in that region are on the order of 20 erg/cm^2/s.

This would imply that to the extent that the precipitating ions are present and generating ENAs, those ENAs would not be expected to be strongly structured, spatially. On the other hand, Synnes et al. (1998) demonstrated that incoming protons with energies of a few keV might be expected to "smear out" through charge exchange over spatial scales of a few 100 km, with up to 10% of incoming protons returning back to space as outgoing ENAs. We continue to model this effect to determine its relative contribution to the other scenarios, but believe that the highly spatially structured ENA emissions, with strong boundaries coincident with 630.0 nm emissions observed by MILENA cannot be explained by this effect.

Alternately, we could be seeing ENAs from lower energy TAIs that were energized at higher altitudes above the conjugate hemisphere, and which then propagate to the northern hemisphere, where they appear as predominantly downgoing energetic ions (with some change in pitch angle closer to 90°

due to the magnetic mirror force). In this case, the ENAs we see could be primarily generated from ions that were accelerated over a relatively long pathlength in the conjugate hemisphere, up to several 100 eV or 1 keV, and which then mirror, precipitate, or charge exchange in the northern hemisphere. These ions could generate ENAs via charge exchange which would then be scattered from atmospheric neutrals up into the VISIONS detector.

This scenario is consistent with the local, *in situ* observations of primarily downgoing and transverse energetic ions at the polar cap boundary. The main problem with it is the inferred potential drop of ~1 keV above the spacecraft where the TAIs are locally observed by VISIONS [Clemmons et al., 2015]. If ions from the conjugate hemisphere fell through this potential drop, they would have a minimum energy of 1 keV, and a maximum energy larger than this. In addition, the bounce time for a keV electron near the polar cap boundary would likely be tens of minutes. Given the time it is expected to take for the initial heating process and upwelling/upflow of the low energy ions to the high-altitude wave-particle acceleration region, there is likely not enough time for these ions to be able to reach the northern hemisphere if they were accelerated in the southern hemisphere.

Figure 8 shows the basic geometry for the "standard picture" (panel A—ENAs generated mostly horizontally in optically thin

region), the "low altitude acceleration" scenario (panel B—wave acceleration region extends into region of dense neutral atmosphere) and the "pressure cooker" scenario, which is described in more detail, below.

The low altitude acceleration scenario would hold if the waves that are presumed to accelerate the TAIs extend to low altitudes (below 400 km, where the mean free path is short). In this case, the neutral density is high enough at these altitudes that any generated ENA would be expected to scatter one or more times before ascending to the optically thin region or being attenuated by the atmosphere to the side or below its generation point. This scenario suffers from the problem that there is a narrow "sweet spot" or range of altitudes where the neutral density is high enough to produce significant ENAs and ENA-neutral scatter without too much attenuation, as well as permitting efficient transverse acceleration by (e.g., BBELF, broadband Extremely Low Frequency) waves, where the wave frequency is several orders of magnitude higher than the ion-neutral collision frequency. Too low an altitude, and the transverse acceleration is not effective, too high and the ENA production and scattering cannot explain the observed upgoing ENAs.

With O+ gyrofrequencies of ~30–40 Hz at VISIONS altitudes, this condition is only satisfied around 350 km altitude (where the ion-neutral collision frequency falls to about 1 Hz). In this scenario, it is possible that the region of wave acceleration would extend to higher altitudes as well, but the ions would have to gain at least 50 eV between about 350 km and where they are observed by MILENA (as low as 400 km). Whalen et al. (1978) did observe a case where TAIs were seen with energies up to 533 eV below 428 km, but the peak in the pitch angle distribution at these altitudes was also just about 90°, suggesting that the particles were either locally accelerated, or near their mirror points after traveling down the field line from a higher altitude acceleration region.

Typical observations of BBELF waves associated with TAIs are generally limited to altitudes above about 600 km [e.g., Arnoldy et al., 1992] although this may be due to the fact that rocket measurements with the necessary instrumentation to observe TAIs typically encounter regions of TAIs and BBELF above 500 km. Indeed, VISIONS only measured intense BBELF waves near its apogee above about 700 km presumably because this is the only location along the trajectory where the payload encountered the localized region of TAIs. The VISIONS rockets did observe intense VLF waves along their entire trajectory (see **Figure 2**) which were associated with the broad regions of energetic electron precipitation essentially present during the entire flight. For low-altitude acceleration, one would expect to see transversely accelerated ions with a range of pitch angles, including upgoing ions. The actual transversely accelerated ions that VISIONS observed near the polar cap boundary were much more intense in the downgoing hemisphere relative to the upgoing hemisphere, suggesting that there was not much acceleration going on below the rocket in that region [Clemmons et al., 2014], although again, we do not have direct measurements of the region that seems to have produced the majority of the ENAs.

In the pressure cooker scenario, first proposed by Gorney et al. (1985), a high-altitude parallel electric field, pointing downwards, reflects upgoing ions back down towards the magnetic mirror point. In this model, the region where waves can transversely accelerate the ions gets traversed multiple times as ions bounce back and forth between the high-altitude potential drop and the magnetic mirror point. This continues until either the ion charge exchanges or gains enough energy to overcome the potential barrier and escapes (or until time variations in the electric potential remove the "lid" from the pressure cooker). This scenario decouples the wave-particle interaction region from the ENA production region, and can *in principle* explain the VISIONS observations. The analysis of these observations is as yet incomplete, and we have not been able to test whether a pressure cooker scenario exists in the remotely-sensed ENA production region.

It will be important for future studies to determine under what conditions and over how large a spatiotemporal extent pressure cooker geometries may exist, as they can dramatically affect the total ion outflow rate and characteristic energy of the outflowing ions.

More detailed modeling is needed in future to determine if this process is in fact operating during the VISIONS launch. The *in situ* measurements do suggest that the pressure cooker is operational in the region of ion acceleration that VISIONS directly flew through [Clemmons et al., 2014]—the high energy precipitating ion population above about 5 keV shown in **Figure 2** narrows and intensifies in the region of transverse ion acceleration, implying a downwards parallel electric field above the rocket. This implies that VISIONS flew through a local pressure cooker, though it is not likely the same region that produced the majority of the ENAs seen by the MILENA instrument.

4.2 Altitudinal Dependence of ENAs Observed in the Polar Cap

Synnes et al. (1998) modeled escaping ENA production as a function of altitude for the case of energetic precipitating protons. For precipitating protons of 1–20 keV, similar to those observed by VISIONS, and for magnetic tilt angle between 10 and 20° (matching the VISIONS geometry), their model predicts a broad altitude range of production for ENAs that eventually escape. For 2 keV precipitating protons, the predicted escaping ENA production altitude distribution had a sharp ledge near 250 km, and a two-peak structure, with maxima near 285 and 560 km. The double-peak structure was explained as due to efficient charge exchange at high altitudes producing the high altitude peak, with many of the ENAs thus produced traveling downwards, until they are re-ionized, scattered in pitch angle, and then produce additional ENAs at lower altitude. At 20 keV energy for the precipitating protons, their model predicts a single peak near 340 km in the altitude profile of escaping ENAs, with FWHM ~300 km. C:son Brandt et al. (2001) modeled the ENA production altitude for 100 eV ions as a function of ion "injection" height, and showed that for ions injected near 400 km, the ENA emissions should come from a thin altitudinal layer, about 100 km wide.

VISIONS traversed the altitude range from below the exobase up to 750 km, returning the first altitude-resolved low energy

ENA measurements in this region. The horizontal ENA fluxes as a function of altitude exhibit a single broad maximum at about 350 km. The VISIONS altitudinal profile is single-peaked, and broader (FWHM is >500 km) than either the idealized model of C:son Brandt et al. (2001) or the model of Synnes et al. (1998). This is likely due to two effects: broader pitch-angle distributions of the energetic ions, and subsequent ENA-neutral scattering. A broader pitch-angle distribution would tend to produce more ENAs at higher altitudes, compared to their modeled cases of 180° pitch angle. Subsequent ENA-neutral scattering following the initial charge exchange would tend to broaden the altitude profile and extend it to lower altitudes, until the ENA mean free path becomes significantly shorter than the distance to the rocket payload (in **Figure 5**, this occurs somewhere between 300 and 400 km). The fact that there are significant horizontal ENAs detected at lower altitudes (below typical mirror heights) implies that the ENA-neutral scattering process is important. This lends further support to the hypothesis that the ions and neutrals are interacting at low altitudes.

In addition to providing some validation for the use of the "thin shell" approximation to trace the ENA emissions to potential source regions, the altitude dependence of the ENA emissions provides important constraints on the energetic ion populations. For example, the energy spectra of the horizontal ENAs detected in the "optically thin" altitude range above 400 km should closely track the energy spectra of the parent ions, since there is very little ENA-neutral scattering at these altitudes over the few 100 km separating the source region from the rocket. The ENAs exhibit an approximate power law spectrum with slope −0.3. VISIONS ion measurements near the polar cap boundary along the rocket track are consistent with this slope in the energy range 50–500 eV [Clemmons et al., 2014]. The horizontal ENAs at high altitude should be more directly proportional to the outflowing ion flux, especially at energies above that of any hypothesized "lid" to the pressure cooker. In contrast, the upgoing ENAs observed earlier in the flight and the low-altitude horizontal ENAs are indicative of the total energetic ion population (though not simply proportional, due to the strong effects of ENA-neutral scattering).

4.3 Total Ion Outflow Over the Sampled Region

To estimate the ion outflow associated with this event, we assume the "horizontal" ENAs detected by MILENA in the polar cap have not undergone any scattering or attenuation at altitudes above 500 km (since the horizontal distance is significantly less than the ~1,000 km mean free path), and that the energetic ions that give rise to these ENAs have pitch angles near 90°. If we assume the horizontal scale size of the ENA producing region is ~200 km (based on the width of the 630.0 nm auroral feature), and that the ENAs are oxygen (O+-O charge exchange cross section at 50 eV approximately 24×10^{-16} cm^2 (Lindsay and Stebbings, 2005)), and that the O density at 500 km is ~6×10^6 cm^3, based on the NRL MSIS-E-90 Atm model (Picone et al., 2002), we can estimate the ion flux that produces the horizontal ENAs seen by VISIONS, using the "optically thin" approximation (Roelof, 1997):

$$j_{ena} = \int dl\, j_{ion}\, \sigma\, n \qquad (1)$$

where σ is the charge exchange cross section, n is the neutral density (assumed pure O), and j_{ena} and j_{ion} are the ENA and ion fluxes, respectively, and the integral is over the line of sight between the ENA source region and the observer (assume $j_{ion} = 0$ outside of this region).

Based on the MILENA calibrations, the peak count rate of 5,000 counts/s corresponds to an ENA flux of ~7.5×10^7 neutrals/s/cm^2/sr. This ENA flux at 50 eV can be directly compared to that reported from Astrid measurements in the polar cap by C:son Brandt et al. (2000). Astrid saw ENA fluxes between 0.1 and 13 keV of 10^6 neutrals/s/cm^2/sr.

Taking into account the presumed ENA source region size and the mean free path for charge exchange in **Eq. 1**, we estimate an average ion flux in the source region (at 50 eV) of 2.6×10^8 ions/s cm^2/sr/dE/E. Assuming the parent ions have pitch angles within ± 15° of 90, this results in an estimate for the total ion flux of 5.5×10^8 ions/s/cm^2, similar to that previously reported by other researchers [e.g., Yau et al., 1983], and in line with the superposed epoch analysis of Wilson et al. (2004) as well as the FAST observations reported in Tung et al. (2001).

This inferred ion flux is ~×100 stronger than the more modest fluxes of transversely accelerated ions observed by VISIONS at the polar cap boundary [Clemmons et al., 2015]. This implies that the observed ENAs cannot be accounted for by the directly measured ions encountered by VISIONS. Instead, the majority of the ENA production was likely occurring to the southwest of the rocket, in the region not directly sampled by the *in situ* measurements. When integrated over the presumed ion source region, and over the ~60 min timescales measured in Wilson et al. (2004), this corresponds to ~20 kg of outflowing oxygen ions. This estimate is a lower limit, because we have not included ions at other pitch angles or other energies.

4.4 Spatial Localization of ENAs and Strong Correlation With 630.0 nm Emissions

The VISIONS MILENA data demonstrate that the low energy ENAs (50 eV) are strongly structured in longitude and latitude. The majority of these ENAs appear to emanate from a region to the southwest of the rocket trajectory. This is also the region where there are large-scale, intense auroral emissions, including strong 630.0 nm emissions. As described above, the IMAGE LENA results of Wilson et al. [2004] provided evidence consistent with a spatially broad, time varying (predominantly diurnal, but also depending on geomagnetic activity) background low energy ENA signal (including upgoing ENAs) at high latitudes. It is important to understand why these results seem so different. The differences are twofold: 1) higher resolution of VISIONS; and 2) targeted launch of VISIONS into an auroral substorm.

VISIONS had a horizontal velocity of 1–2 km/s, as opposed to the IMAGE perigee velocities of >8 km/s. Increasing the "dwell time" in the region of interest from 2 to 3 min (IMAGE) to ~15 min allowed VISIONS to sample the temporal variation of ion outflow over a significant fraction of the substorm life-cycle.

This slow velocity also increased the ENA image spatial and temporal resolution—MILENA produced a full sky image every second (every 1.5 km along track), and full energy distributions in 3-D every 16 s (24 km along track), compared to IMAGE, which had a 2-min spin period, and produced full-sky images every ~1,000 km along track near perigee. VISIONS also had the capability to resolve energies of the incoming ENAs, which IMAGE LENA lacked. This allows VISIONS to discriminate between, e.g., 50 eV ENAs and the lower energy "rammed" population, which may produce counts with significant angular scatter in the instrument.

Regarding the conditions under which VISIONS made its measurements—VISIONS was launched into an active aurora ~30 min after substorm onset. While IMAGE made ~130 perigee passes over the 3 months of data described in Wilson et al. (2004), these ranged over local times from dawn-dusk to noon-midnight. Also, while they were all in the local (southern) winter, each perigee pass was only in the nightside auroral zone for 2–3 min, every 14.2 h. This low duty cycle made it very unlikely for IMAGE LENA to directly observe substorm outflow near perigee within 30 min after onset. Thus, the IMAGE LENA data represents a climatology of the hot oxygen environment during quiet conditions, rather than representing the substorm response.

The main limitation of the thin shell tracing is that, due to scattering effects, it may produce significant errors in quantitatively estimating ion flux from measured upgoing ENA flux, and it does not provide detailed knowledge of the ion populations that produced the ENAs, primarily due to ENA-neutral scattering. Nonetheless, it is extremely useful in providing the first high resolution localization of the regions where significant ion acceleration is occurring at low altitudes in the ETR. Future efforts will need to self-consistently model ion and neutral populations to better understand the limitations and accuracies of the thin-shell approach, and improve our techniques for obtaining ion flux information from the ENA measurements.

4.5 Summary

The VISIONS sounding rocket provided the first height-resolved, high-resolution measurements of low energy neutral atoms (<1 keV) associated with transversely accelerated ions in the nightside auroral zone following substorm onset. The ENA emissions were most intense in the auroral zone, and were dominated there by upgoing ENAs, indicating a strong interaction between the energetic ions and the neutral atmosphere. The ENAs exhibited a strong altitudinal dependence, maximizing around 400 km "Thin shell" mapping of the ENAs to an idealized source region at 375 km revealed a strong association between 50 eV ENA emission and regions of strong 630.0 nm auroral emissions. The region of ENA production was well structured and had a long-term coherence over the ~10 min of observation. The estimated ion flux (for the component that leads to charge exchange and ENA generation) from the region of strong ENA emissions was ~5.5 × 10^8 ions/s cm^2, and the ENA energy spectrum is consistent with a power-law with slope −0.3.

The *in situ* measurements detected a narrow region of transversely associated ions near 700 km altitude that were precisely observed in a localized region of enhanced broadband ELF waves suggesting that strong wave-particle interactions near the O$^+$ gyro frequency may have been operating to accelerate the oxygen ions.

The observations suggest that there exist large (~200 km horizontally) regions of efficient wave particle heating up to a few keV. Further work is needed to model the ion energization observed by VISIONS, and to produce simulated ENA images for comparison, as well as to model the ion acceleration and propagation to assess how much of the ion population ends up escaping to high altitudes, and how much is lost to charge exchange and precipitation.

ADDITIONAL REQUIREMENTS

For additional requirements for specific article types and further information please refer to Author Guidelines.

DATA AVAILABILITY STATEMENT

The raw data supporting the conclusions of this article can be downloaded from: https://doi.org/10.5281/zenodo.6326353.

AUTHOR CONTRIBUTIONS

FUNDING

ACKNOWLEDGMENTS

REFERENCES

Arnoldy, R. L., Lynch, K. A., Kintner, P. M., Vago, J., Chesney, S., Moore, T. E., et al. (1992). Bursts of Transverse Ion Acceleration at Rocket Altitudes. *Geophys. Res. Lett.* 19 (4), 413–416. doi:10.1029/92gl00091

Barabash, S., Brandt, s., Norberg, R. Lundin, O. E. C., Mauk, C. J. C. B. H., and Koskinen, H. (1997). Energetic Neutral Atom Imaging by the Astrid Micro Satellite. *Adv. Space Res.* 20. doi:10.1016/s0273-1177(97)00560-7

Bazell, D., Roelof, E. C., Sotirelis, T., Brandt, P. C., Nair, H., Valek, P., et al. (2010). Comparison of TWINS Images of Low-Altitude Emission of Energetic Neutral Atoms with DMSP Precipitating Ion Fluxes. *J. Geophys. Res.* 115, a–n. doi:10.1029/2010JA015644

Brandt, P., Barabash, S., Roelof, E. C., Chase, C. J., and Wilson, G. R. (2000). Energetic Neutral Atom Imaging at Low (≤10 keV) Energies from Astrid: Observations and Simulations. *J. Atmos. Solar-Terrestrial Phys.* 62, 901–909. doi:10.1016/s1364-6826(00)00040-7

Brandt, P. C., Barabash, S., Roelof, E. C., and Chase, C. J. (2001). Energetic Neutral Atom Imaging at Low Altitudes from the Swedish Microsatellite Astrid: Observations at Low (≤10 keV) Energies. *J. Geophys. Res.* 106 (A11), 24663–24674. doi:10.1029/2000ja000119

Carlson, C. W., Curtis, D. W., Paschmann, G., and Michael, W. (1983). An Instrument for Rapidly Measuring Plasma Distribution Functions with High Resolution. *Adv. Space Res.* 2, 67.

Chappell, C. R., Moore, T. E., and Waite, J. H. (1987). The Ionosphere as a Fully Adequate Source of Plasma for the Earth's Magnetosphere. *J. Geophys. Res.* 92 (A6), 5896–5910. doi:10.1029/JA092iA06p05896

Chaston, C., Bonnell, J., Carlson, C., McFadden, J., Ergun, R., Strangeway, R., et al. (2004). Auroral Ion Acceleration in Dispersive Alfvén Waves. *J. Geophys. Res.* 109 (A04205). doi:10.1029/2003ja010053

Clemmons (2014) Paper to Be Submitted Describing VISIONS Pressure Cooker *In Situ* Measurements

Collier, M. R., Chornay, D., Clemmons, J., Keller, J. W., Klenzing, J., Kujawski, J., et al. (2015). VISIONS Remote Observations of a Spatially-Structured Filamentary Source of Energetic Neutral Atoms Near the Polar Cap Boundary during an Auroral Substorm. *Adv. Space Res.* 56, 2097–2105. doi:10.1016/j.asr.2015.08.010

Fok, M.-C., Moore, T. E., Wilson, G. R., Perez, J. D., Zhang, X. X., Brandt, P. C. S., et al. (2003). Global ENA Image Simulations. *Space Sci. Rev.* 109, 77–103. doi:10.1023/b:spac.0000007514.56380.fd

Fuselier, S. A., Ghielmetti, A. G., Moore, T. E., Collier, M. R., Quinn, J. M., Wilson, G. R., et al. (2001). Ion Outflow Observed by IMAGE: Implications for Source Regions and Heating Mechanisms. *Geophys. Res. Lett.* 28 (6), 1163–1166. doi:10.1029/2000gl012450

Glocer, A., Toth, G., Gombosi, T., and Welling, D. (2009). Modeling Ionospheric Outflows and Their Impact on the Magnetosphere, Initial Results. *J. Geophys. Res.* 114 (A5), A05216. doi:10.1029/2009ja014053

Glocer, A., Welling, D., Chappell, C. R., Toth, G., Fok, M. C., Komar, C., et al. (2020). A Case Study on the Origin of Near-Earth Plasma. *J. Geophys. Res. Space Phys.* 125 (11), 1–19. doi:10.1029/2020JA028205

Gloeckler, G., and Hamilton, D. C. (19871987). AMPTE Ion Composition Results. *Phys. Scr.* T18, 73–84. Number T18. doi:10.1088/0031-8949/1987/T18/009

Gorney, D. J., Chiu, Y. T., and Croley, D. R. (1985). Trapping of Ion Conics by Downward Parallel Electric fields. *J. Geophys. Res.* 90, 4205. doi:10.1029/ja090ia05p04205

Haaland, S., Eriksson, A., Engwall, E., Lybekk, B., Nilsson, H., Pedersen, A., et al. (2012a). Estimating the Capture and Loss of Cold Plasma from Ionospheric Outflow. *J. Geophys. Res.* 117, a–n. doi:10.1029/2012JA017679

Haaland, S., Li, K., Eriksson, A., André, M., Engwall, E., FöRster, M., et al. (2012b). "Cold Ion Outflow as a Source of Plasma for the Magnetosphere," in *Dynamics of the Earth's Radiation Belts and Inner Magnetosphere*. Editors D. Summers, I. R. Mann, D. N. Baker, and M. Schulz and, 341–354. doi:10.1029/2012GM001317

Hecht, J. H., Strickland, D. J., and Conde, M. G. (2006). The Application of Ground-Based Optical Techniques for Inferring Electron Energy Deposition and Composition Change during Auroral Precipitation Events. *J. Atmos. Solar-Terrestrial Phys.* 68, 1502–1519. doi:10.1016/j.jastp.2005.06.022

Hecht (2014). *Paper to Be Submitted Describing VISIONS RAI Observations of O/N2 Depletions*.

Huddleston, M. M., Chappell, C. R., Delcourt, D. C., Moore, T. E., Giles, B. L., and Chandler, M. O. (2005). An Examination of the Process and Magnitude of Ionospheric Plasma Supply to the Magnetosphere. *J. Geophys. Res.* 110 (A12), A12202. doi:10.1029/2004JA010401

Jensen, M. D., and Baker, K. D. (1992). Measuring Ionospheric Electron Density Using the Plasma Frequency Probe. *J. Spacecraft Rockets* 29 (1), 91–95. doi:10.2514/3.26318

Kindel, J. M., and Kennel, C. F. (1971). Topside Current Instabilities. *J. Geophys. Res.* 76, 13.

Kintner, P. M., Bonnell, J., Arnoldy, R., Lynch, K., Pollock, C., and Moore, T. (1996). SCIFER-transverse Ion Acceleration and Plasma Waves. *Geophys. Res. Lett.* 23 (14), 1873–1876. doi:10.1029/96gl01863

Kozyra, J. U., Cravens, T. E., and Nagy, A. F. (1982). Energetic O+ Precipitation. *J. Geophys. Res.* 87, 2481.

Lindsay, B. G., and Stebbings, R. F. (2005). Charge Transfer Cross Sections for Energetic Neutral Atom Data Analysis. *J. Geophys. Res.* 110, A12213. doi:10.1029/2005JA011298

Lynch, K. A., Arnoldy, R. L., Kintner, P. M., and Bonnell, J. (1996). The AMICIST Auroral Sounding Rocket: A Comparison of Transverse Ion Acceleration Mechanisms. *Geophys. Res. Lett.* 23 (23), 3293–3296. doi:10.1029/96gl02688

Moore, T., Chandler, M., Pollock, C., Reasoner, D., Arnoldy, R., Austin, B., et al. (1996). Plasma Heating and Flow in an Auroral Arc. *J. Geophys. Res.* 101 (A3), 579. doi:10.1029/95ja03154

Moore, T. E., et al. (2000). "The Low Energy Neutral Atom Imager for IMAGE," in *The IMAGE Mission*. Editor J. L. Burch (Dordrecht, Netherlands: Kluwer Academic Publishers).

Picone, J. M., Hedin, A. E., Drob, D. P., and Aikin, A. C. (2002). NRLMSISE-00 Empirical Model of the Atmosphere: Statistical Comparisons and Scientific Issues. *J. Geophys. Res.* 107, 151468–151471. doi:10.1029/2002JA009430

Roelof, E. C. (1987). Energetic Neutral Atom Image of a Storm-Time Ring Current. *Geophys. Res. Lett.* 14, 652–655. doi:10.1029/gl014i006p00652

Roelof, E. C. (1997). Energetic Neutral Atom Imaging of Magnetospheric Ions from High- and Low-Altitude Spacecraft. *Adv. Space Res.* 20, 341–350. doi:10.1016/s0273-1177(97)00689-3

Roelof, E. C., and Skinner, A. J. (2000). Extraction of Ion Distributions from Magnetospheric ENA and EUV Images. *Space Sci. Rev.* 91, 437–459. doi:10.1007/978-94-011-4233-5_15

Rowland, D. E. (2011). Science of Opportunity: Heliophysics on the FASTSAT Mission and STP-S26. *IEEE Aerospace Conf. Proc.* 2011. March 5-12. doi:10.1109/aero.2011.5747235

Shelley, E. G., Johnson, R. G., and Sharp, R. D. (1972). Satellite Observations of Energetic Heavy Ions during a Geomagnetic Storm. *J. Geophys. Res.* 77 (31), 6104–6110. doi:10.1029/JA077i031p06104

Söraas, F., Lindalen, H. R., Måseide, K., Egeland, A., Sten, T. A., and Evans, D. S. (1974). Proton Precipitation and the Hβ Emission in a Postbreakup Auroral Glow. *J. Geophys. Res.* 79, 1851–1859. doi:10.1029/ja079i013p01851

Synnes, S. A., Søraas, F., and Hansen, J. P. (1998). Monte-Carlo Simulations of Proton aurora. *J. Atmos. Solar-Terrestrial Phys.* 60, 1695–1705.

Torr, M. R., Walker, J. C. G., and Torr, D. G. (1974). Escape of Fast Oxygen from the Atmosphere during Geomagnetic Storms. *J. Geophys. Res.* 79, 5267–5271. doi:10.1029/ja079i034p05267

Tung, Y.-K., Carlson, C. W., McFadden, J. P., Klumpar, D. M., Parks, G. K., Peria, W. J., et al. (2001). Auroral Polar Cap Boundary Ion Conic Outflow Observed on FAST. *J. Geophys. Res.* 106, 3603–3614. doi:10.1029/2000ja900115

Welling, D. T., Jordanova, V. K., Glocer, A., Toth, G., Liemohn, M. W., and Weimer, D. R. (2015). The Two-way Relationship between Ionospheric Outflow and the Ring Current. *J. Geophys. Res. Space Phys.* 120, 4338–4353. doi:10.1002/2015JA021231

Whalen, B. A., Bernstein, W., and Daly, P. W. (1978). Low-altitude Acceleration of Ionospheric Ions. *Geophys. Res. Lett.* 5, 1. doi:10.1029/gl005i001p00055

Wilson, G., Moore, T., and Collier, M. (2003). Low-energy Neutral Atoms Observed Near the Earth. *J. Geophys. Res.* 108 (A4). doi:10.1029/2002ja009643

Wilson, G., Ober, D., Germany, G., and Lund, E. (2004). Nightside Auroral Zone and Polar Cap Ion Outflow as a Function of Substorm Size and Phase. *J. Geophys. Res.* 109 (A02206). doi:10.1029/2003ja009835

Yau, A. W., Whalen, B. A., McNamara, A. G., Kellogg, P. J., and Bernstein, W. (1983). Particle and Wave Observations of Low-Altitude Ionospheric Ion Acceleration Events. *J. Geophys. Res.* 88, 341. doi:10.1029/ja088ia01p00341

Zettergren, M., Semeter, J., Blelly, P.-L., and Diaz, M. (2007). Optical Estimation of Auroral Ion Upflow: Theory. *J. Geophys. Res.* 112, a–n. doi:10.1029/2007JA012691

Publisher's Note: All claims expressed in this article are solely those of the authors and do not necessarily represent those of their affiliated organizations, or those of the publisher, the editors, and the reviewers. Any product that may be evaluated in this article, or claim that may be made by its manufacturer, is not guaranteed or endorsed by the publisher.